Methodology for small animals targeted irradiations at conventional and ultra-high dose rates 65 MeV proton beam

Manon Evin, Charbel Koumeir, Arthur Bongrand, Grégory Delpon, Ferid Haddad, Quentin Mouchard, Vincent Potiron, Gaëlle Saade, Noël Servagent, Daphnée Villoing, et al.

Physica Medica 120 (2024) 103332

Contents lists available at ScienceDirect

Physica Medica

journal homepage: www.elsevier.com/locate/ejmp

Original paper

Methodology for small animals targeted irradiations at conventional and ultra-high dose rates 65 MeV proton beam

Manon Evin [a,*], Charbel Koumeir [a,b], Arthur Bongrand [b,c], Gregory Delpon [a,c], Ferid Haddad [a,b], Quentin Mouchard [a], Vincent Potiron [c,d], Gaëlle Saade [d], Noël Servagent [a], Daphnée Villoing [c], Vincent Métivier [a], Sophie Chiavassa [a,c]

[a] Nantes Université, IMT Atlantique, CNRS/IN2P3, SUBATECH, F-44000 Nantes, France
[b] GIP ARRONAX, Saint-Herblain, France
[c] Institut de Cancérologie de l'Ouest, site de Saint-Herblain, France
[d] Nantes Université, CNRS, US2B, UMR 6286, F-44000 Nantes, France

ARTICLE INFO

Keywords:
Dosimetry
Monte Carlo simulation
Preclinical studies
Proton therapy
FLASH radiotherapy

ABSTRACT

As part of translational research projects, mice may be irradiated on radiobiology platforms such as the one at the ARRONAX cyclotron. Generally, these platforms do not feature an integrated imaging system. Moreover, in the context of ultra-high dose-rate radiotherapy (FLASH-RT), treatment planning should consider potential changes in the beam characteristics and internal movements in the animal.

A patient-like set-up and methodology has been implemented to ensure target coverage during conformal irradiations of the brain, lungs and intestines. In addition, respiratory cycle amplitudes were quantified by fluoroscopic acquisitions on a mouse, to ensure organ coverage and to assess the impact of respiration during FLASH-RT using the 4D digital phantom MOBY. Furthermore, beam incidence direction was studied from mice μCBCT and Monte Carlo simulations. Finally, *in vivo* dosimetry with dose-rate independent radiochromic films (OC-1) and their LET dependency were investigated.

The immobilization system ensures that the animal is held in a safe and suitable position. The geometrical evaluation of organ coverage, after the addition of the margins around the organs, was satisfactory. Moreover, no measured differences were found between CONV and FLASH beams enabling a single model of the beamline for all planning studies. Finally, the LET-dependency of the OC-1 film was determined and experimentally verified with phantoms, as well as the feasibility of using these films *in vivo* to validate the targeting.

The methodology developed ensures accurate and reproducible preclinical irradiations in CONV and FLASH-RT without in-room image guidance in terms of positioning, dose calculation and *in vivo* dosimetry.

1. Introduction

The primary consideration for cancer treatment with external beam radiation therapy relies on the dose–response relationship to control both efficacy and toxicities. Hence, accurate information about the dose spatial distribution is critical for preclinical and clinical research in radiotherapy, especially for *in vivo* studies on small animal models, where the perspectives are two-fold and bi-translational (i.e. testing on animals for future applications in humans or using animal models to study the mechanisms observed in humans) [1]. The published guidelines provide requirements for this intended transposition between small animals and humans [2], divided into two categories. On the one hand, a precise and robust targeting method involving, for instance, preclinical patient-like image-guided radiotherapy [3] and respiratory gating [4,5], as well as quality assurance protocols tailored to preclinical platforms [6]. On the other hand, a 3-dimensional dose distribution computation, preferentially in each individual with a coherent spatial distribution, enables the comparison of results between different modalities and inter-centers. Finally, *in vivo* dosimetry protocols should be applied, ensuring the targeting and the agreement between calculated and delivered dose distribution.

In addition to this generic preclinical framework, emerging techniques raise technical challenges. In FLASH radiotherapy (FLASH-RT) [7], for instance, the ultra-high dose rate (UHDR) beams (Dose Rate >

* Corresponding author at: 4 Rue Alfred Kastler, 44300 Nantes, France.
E-mail address: manon.evin@subatech.in2p3.fr (M. Evin).

https://doi.org/10.1016/j.ejmp.2024.103332
Received 26 December 2023; Received in revised form 20 February 2024; Accepted 11 March 2024
Available online 21 March 2024

40 Gy/s, treatment duration of the order of the ms) require the monitoring, or at least the knowledge, of the temporal distribution of the dose [8]. However, to compare different irradiation modes in optimal configuration, the set-ups must be as similar as possible, which can be technically challenging. In general, if clinical machines are used [9–11], the UHDR irradiation does not occur at the isocenter like for conventional radiotherapy (CONV) but closer to the irradiation head (to obtain a sufficient dose rate). Nevertheless, the line configuration strongly influences the beam geometry and the online dosimetry. In contrast, irradiation platforms of research infrastructures often have more flexibility regarding irradiation parameters, such as beam intensity and temporal structures. However, they shall implement a rigorous and reliable set-up and dosimetric environment to complement and compete with clinical robustness.

Since 2019, radiobiology studies have been conducted in the ARRONAX cyclotron irradiation platform, consisting of the horizontal experimental irradiation line and associated online dosimetry methods for protons and helium ions beams of biological interest. In particular, cell survival was first performed with ARRONAX's proton beam [12]. Irradiations on the plateau of zebrafish embryos [13,14] and cells are ongoing at conventional and ultra-high dose rates.

Irradiations of mice are planned to investigate the FLASH effect and its mechanisms further. A previous study used Monte Carlo simulations based on our beamline to investigate the impact of various sources of uncertainty on the proton range and the absorbed dose distribution in the context of preclinical irradiation of small animals in the plateau of the Bragg curve [15]. Moreover, currently, the ARRONAX beamline does not include an on-board imager, making positioning of the mouse (healthy tissues or tumors) a challenge. To overcome this issue, we have developed a targeting method based on the XRAD225Cx (Precision X-Ray Inc. in CT, USA) preclinical irradiator [3] and an immobilization system similar to those used in clinical routine. Considered organs of interest are the brain, the lungs and the intestines, which are often used to study the effects of radiation on healthy tissue and have recently been used to demonstrate the tissue-sparing effect of FLASH–RT [7,16,17]. The absorbed dose distribution is calculated for each mouse for the ARRONAX proton beam with the Monte Carlo GATE code on μCBCT images from XRAD225Cx device (Precision X-Ray Inc. in CT, USA).

The present study evaluates our repositioning method and determines the margins to ensure satisfactory target organ coverage. In addition, the study first assesses the impact of the respiratory cycle in the context of FLASHT-RT studies, where the irradiation time is very brief (millisecond) compared to animal respiratory movements. The selection of the maximal target size relies on dose homogeneity optimization for two beam angles.

Finally, the study validates the feasibility of *in vivo* dosimetry using OC-1 (OrthoChrome) radiochromic films with appropriate Linear Energy Transfer (LET) correction.

2. Materials and methods

2.1. Preclinical beamlines and dosimetric environment

ARRONAX is an isochronous cyclotron (IBA Cyclone 70XP), delivering proton up to 70 MeV at the exit window, with beam intensity up to 375 μA on target. The achievable dose rate ranges from 0.1 Gy/s up to a few hundred kGy/s, depending on the set-up requirements regarding beam size and homogeneity. An electrostatic pulsing system enables macro-pulsing, creating various temporal structures [18]. ARRONAX experimental hall features two irradiation beamlines suitable for radiobiology: horizontal [15] and vertical. The general global structure was previously presented [15] and sketched in Fig. 1a. The size of the homogeneous field is defined by the dose above 80 % of the maximum dose, excluding the penumbra zone, which is between 80 % and 20 % of the maximum dose. Hence, the collimator aperture must be enlarged by the penumbra size to obtain the required homogeneous field at the target position. This geometric penumbra, resulting from the collimation of a divergent beam, increases with the distance between the collimator and with the collimator aperture. The size and shape of the collimator can be adjusted manually to an accuracy of 0.1 mm. The distance between the collimator and the target is set to 4 cm, providing the best compromise between lateral and distal homogeneity, together with reduced geometric penumbra [19]. The collimator aperture (C) in the plane orthogonal (x,y) to the beam trajectory is linked to the optimal homogeneous field size (F) and the geometric penumbra (P) at a distance d from the collimator by the Eq. (1):

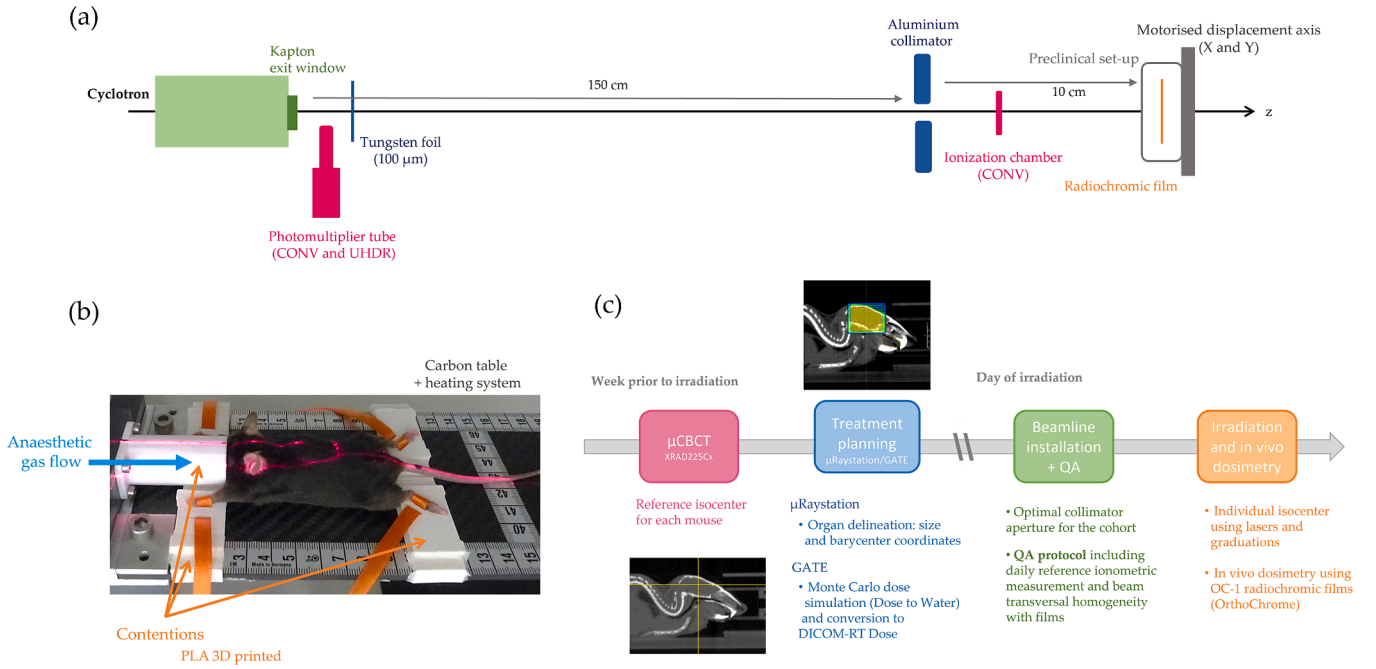

Fig. 1. (a) Schematical view of the ARRONAX irradiation beamline; (b) Photograph of the positioning system (3D-printed immobilization system and graduations); (c) Workflow diagram.

$$C(x,y) = F(x,\ y) + P(x,y,d) \quad (1)$$

with

$$F(x,y) = O(x,y) + m_T\ (x,y) \quad + \ m_R(x,y) \quad (2)$$

The optimal homogeneous field size (F) for a mouse whose organ size (O) is increased by the targeting margins (m_T), taking into account the positioning accuracy, and by the respiratory margins (m_R), correcting for the fact that μCBCT gives an average volume which can lead to significant coverage losses of the moving volume, particularly during very brief UHDR irradiation (Method 2.3).

The mouse positioning system, shown in Fig. 1b, consists of a patient-like 3D-printed (PLA) harmless immobilization system clipped to the carbon treatment couch. A close-up photograph and a 3D modelling view are available in Supplementary material (Suppl. Fig. S1). The modules for the upper and lower body parts are independent, and the distance between them in the feet direction can be adapted to the size of each animal. Graduations, used as external markers for the lasers, are bonded to the carbon couch, guaranteeing the repositioning of the modules and the animal. Regarding contentions, four ribbons are secured through dedicated slots and are used to place the mouse's paws outside the irradiation field without injury and in a reproducible position. In addition, anaesthesia is required because the strips do not prevent intentional movements. The anaesthetic gas is supplied through the printed muzzle module. As yet, the platform does not feature an online imaging system; this study presents a method for enabling the delivery of accurately targeted irradiations without image guidance, according to the workflow diagram presented in Fig. 1c. The graduated carbon couch prone to activation has been duplicated to meet radiation safety precautions. The light material of the thin support system is rarely directly in the irradiation field; whenever it is, activation goes down to background value on few hours post-irradiation. The imaging system used to acquire the planning μCone beam Computed Tomography (μCBCT) is an XRAD225Cx irradiator (Precision X-Ray Inc. in CT, USA). The nominal voltage is 40 kV, and the intensity is 1.5 mA. Three millimeters of aluminum filtration is added for image quality [3]. The μCBCT imaging dose to mice is around 0.3 Gy [2]. The size of the voxels has been fixed at $0.2 \times 0.2 \times 0.2\ mm^3$ to guarantee a satisfactory spatial resolution and limit the errors during dose calculations [15]. The μCBCT acquired by XRAD225Cx can be transferred to μRaystation 8B (RaySearch Laboratories, Stockholm, Sweden) Treatment Planning System (TPS) adapted to small animals. Specifically, this software allows organ delineation and image registration to evaluate repositioning precision [20].

2.2. Monte Carlo simulations

Our beamline model published by Bongrand *et al.* [15] runs on the GATE code v9.1 (2021) based on Geant4-10.07 (December 2020) [21]. The model uses the recommended physics list of hadronic interactions QGSP_BIC_EMZ [22]. The primary proton source is an elliptical beam (FWHM in x and y directions, respectively 2 and 3 mm) placed in a vacuum 10 μm before the Kapton window at the end of the beamline. To reduce the calculation time, a secondary source was simulated as phase space at the end of the individual independent part before the collimator. The simulated dose was recorded in terms of Dose to Water in coherence with experimental dose measurements and clinical practices. Lateral and distal distributions have been validated with radiochromic films (OC-1) and a calibrated ionization chamber (PTW Advanced Markus, $N_{D,w} = 1.549$ Gy/nC) respectively. Beam energy and spread have been characterized to 67.5 ± 0.35 (1 σ) MeV. In Fig. 1a, the beam energy spectrum at the target entrance level is 64.7 ± 0.50 MeV. Cut production for secondary particles has been set to 1 mm in all geometries and 0.1 mm within the collimator and in the target. The maximal step size chosen was 0.1 mm in the target and 1 mm outside the target [15,23]. The number of protons simulated was set to keep the mean statistical uncertainty below 2 % within the region of interest.

To perform the Monte Carlo simulation on the animal images acquired with the XRAD225Cx, an automatic segmentation method has been previously developed [24], allowing the determination of 125 tissues interpolated from 34 ICRU tissues (ICRU44, ICRU 46) [25,26]. The validity of the method for 68 MeV protons has been previously shown [15]. Moreover, to reduce statistical noise, dose distributions in mice and films are filtered with a median filter with a kernel of 3 pixels [27].

2.3. Methodology for organ targeting without image guidance

2.3.1. Evaluation of the positioning system and targeting margins

The targeting accuracy was assessed by resetting an anaesthetized (isoflurane gas) C57BL/6 mouse for the brain, lungs, and intestines ten times split between two operators with the lasers and without image guidance. Each time, a μCBCT was acquired using the XRAD225Cx. The lungs and the intestines were targeted using the graduations on the table. Whereas, for the brain, an ear was used as an external marker, which results in an improved head position with the muzzle supported by the anaesthesia nozzle and, in particular, fewer rotations that can lead to loss of brain coverage. The organ delineation was performed on μRaystation software, and maximal organ dimensions in each direction were recorded. For the best possible reproducibility, organ contouring was based on bone structures for the brain and abdomen and grey level thresholding ([-850, −250] HU) for the lungs. The TPS μRaystation was also used to perform rigid registrations without rotation with respect to the reference image. The offsets of the organ barycenters between the reference and repositioning images were used to quantify the positioning accuracy without imaging. These distances are applied around the organs in each direction, defining the targeting margins.

2.3.2. Respiratory margins

The XRAD225Cx fluoroscopic mode (7.5 image/s) was used to measure the respiratory cycle amplitudes between the two extreme phases of respiration, full inspiration and full expiration, with our anaesthesia and contention set-up. In this study, ten respiratory cycles were measured on the fluoroscopic images of a mouse. In the three directions, the distances between full expiration and full inspiration constitute the respiratory margins.

2.3.3. Geometrical organ coverage

Regarding organ geometrical coverage, calculated margins do not consider animal rotations. In order to verify that these margins ensure the organ's coverage, a box modelling the optimal homogenous field size for each localization was created and applied on all ten repositioning on μRaystation.

2.4. Impact of the dose delivery modality and the beam incidence

2.4.1. Conventional versus FLASH: Impact on beam characteristics and dosimetry impact of respiration

In order to compare CONV and FLASH irradiation modes in ongoing biological studies, the beam geometry and energy spectrum were experimentally characterized. These measurements are presented and compared with the Monte-Carlo simulation model of the beamline. First, the code's ability to reproduce the beam geometry was investigated through lateral beam profiles measured with radiochromic OC-1. The simulation was then used to assess other experimental set-ups and characterize the induced geometric penumbra caused by the collimation. The profile edge degradation must be considered to determine the collimator size in a specific set-up to ensure lateral homogeneity in the required field size. Moreover, the depth dose profile was measured to ensure that machine settings did not change the beam's energy spectrum. The measurement was performed in a water tank with the Markus Advanced chamber (PTW type 34045) at CONV and FLASH settings. In order to use the chamber for both modalities, the mean dose rate of

FLASH was reduced to 0.2 Gy/s, as for the CONV, using the pulsing system [18] with shorter macro-pulses and a lower frequency while keeping the ultra-high dose rate in the pulse. So, the chamber's response is not significantly impacted since the charge in the micro-pulse is relatively low (<0.1 Gy), and the macro-pulses are quite far apart (50 ms) about the drift time of the ions in the chamber (20 μs) [28].

Moreover, to assess the potential influence of breathing and tissue variations that can induce a substantial dosimetric impact in medium-energy proton therapy, a digital phantom was generated from measured amplitudes and densities. The 4D MOBY (Mouse Whole Body) digital phantom was developed by Segars et al. in 2004 [29], initially for nuclear medicine dosimetry applications. Recently, this model has been used in external radiation therapy to evaluate the consequences of moving lung tumors [30]. The second version of the software (MOBYv2) was used in this study to quantify the influence of the changes in volume, density and composition of the lungs during respiration in the context of FLASH-RT, where the short irradiation time (<millisecond) can arise anytime during the cycle.

The maximal amplitude measured on the XRAD225Cx between full inspiration and full expiration were considered to generate two numerical phantoms. The isotropic voxel size is 0.2 mm, as on the μCBCTs. The tissue mass densities and compositions are allocated using three ICRU tissues [25] (muscle 1.05 g/cm^3, cortical bone 1.92 g/cm3, inflated lungs 0.26 g/cm^3) and regarding deflated lungs density, patient mean lung density from full expiration dosimetric CT (0.45 g/cm^3) have been used instead of the less realistic ICRU Deflated Lung value (1.05 g/cm^3).The absorbed dose distribution in the lungs for full inspiration and full expiration phases has been simulated on GATE for lateral and posterior beam incidences and compared using dose-volume histograms (DVH) from μRaystation.

2.4.2. Impact of the beam incidence (lateral versus posterior)

Eleven C57BL/6 mice (five males and five females aged three months and a male of six months) were weighed and imaged under isofluorane gas anaesthesia to study organ sizes and proportions. In fact, with 65 MeV protons, irradiation of large organs may be limited due to the increase in dose with depth along the Bragg curve. Hence, the dose distribution in the organs was simulated on the mice for which the depth dose heterogeneity seemed acceptable from data on the organ sizes. Finally, the two beam incidences, lateral and posterior, were compared using the HI98 homogeneity index.

($HI98 = \frac{D_{2\%} - D_{98\%}}{D_{50\%}}$, with $D_{x\%}$ the dose received by x% of the volume) for targets. Regarding organs at risk in the irradiation field, the mean dose will be used for the buccal cavity and the heart and the maximum dose given $D_{2\%}$ for the spinal cord.

2.5. In vivo dosimetry

In vivo dosimetry ensures the targeting and the agreement between calculated and delivered dose distribution. Radiochromic films OC-1 are used for FLASH-RT studies because of their dose-rate independence [31]. However, when the films are placed just behind the animal, a saturation of the film response, due to the increase of the Linear Energy Transfer (LET) of protons along the Bragg curve, is likely to appear in the same way as for EBT Gafchromic films (up to 20 % in the peak region) [32]. To characterize this LET dependency, a depth dose profile was acquired with OC-1 films and a calibrated ionization chamber PTW Advanced Markus (PTW type 34045) and TRS-398 formalism [33] in RW3 slabs. The dose-averaged LET (LET_d) will be considered according to the recommendation for protons LET simulations on the Bragg peak region [34] and to be consistent with the literature. Thus, a linear relationship for the LET-dependence, based on the one proposed by Anderson [35] for Gafchromic films EBT3 films, has been computed for our OC-1 films using GATE for LET simulation and experimentally verified with tissue substitute cylinders (Gammex-RMI, WI, USA). This correction was tested with calibrated tissue substitutes and RW3 slabs, whose mass densities and compositions were entered in GATE. Two configurations were tested: (i) Bone B-200 and Adipose for no quenching reference and (ii) Bone B-200 downstream 5 mm of RW3. Information on density and composition are displayed in supplementary material (Suppl. Table S1). Simulated and experimental films are compared using a local gamma-index metric on the clinical software VeriSoft (v8.0.1.0). Moreover, the feasibility of *in vivo* dosimetry with film placed behind the animal was evaluated on a dead mouse in the case of lateral whole brain irradiation with 14 Gy measured with a film placed upstream of the mouse.

3. Results

3.1. Methodology for targeting without image guidance

3.1.1. Evaluation of the positioning system and targeting margins

The system's accuracy in guaranteeing the position of the internal organs targeted without image guidance was assessed on ten imaging sessions. The minimal, mean and maximal offsets in the three directions between the barycenter of the organs of the reference image and the barycenter on the μCBCT acquired repositioning the animal without image guidance are shown in Table 1.

To ensure the target coverage, equivalent margins, referred to as target margins in Eq. (2), should be applied. The margins (m_T) correspond to the observed offsets applied in both directions, i.e. twice the values in Table 1. For the brain, m_T mt equals to 2.8 mm in the right-left direction and 1.2 mm longitudinally for an anteroposterior beam; and equals to 1.8 mm anteroposteriorly and 1.2 mm longitudinally for a lateral beam.

3.1.2. Respiratory margins

Measured maximum amplitudes (full inspiration) relative to full expiration position are 1.7 mm in the longitudinal direction (diaphragm motion) and 0.6 mm in the posterior direction. No changes were observed in the right-left direction. Moreover, the respiration duration, of the order of the second, is long in comparison with FLASH-RT irradiation time (milliseconds). Then, the above amplitudes must be added to the margins in the feet and in the back directions, respectively, to ensure the lung's coverage (m_R, Eq. (2).

3.1.3. Geometrical organ coverage

For each localization, the optimal homogeneous field size is determined by adding targeting and respiratory margins to the organ size (Table 2). More precisely, targeting margins correspond to the shifts observed, applied in both directions and maximal offset values are reported in Table 1. Additional respiratory margins linked to the maximal amplitude of the respiratory cycles are considered for the lungs (1.7 mm in the longitudinal direction,0.6 mm in the posterior direction and no change along the right-left direction).

Regarding organ geometrical coverage, the target volume is always enclosed for the lungs and intestines. However, for the brain, three repositioning images indicated a possible loss of coverage due to head rotations. Uncovered volumes are very small and represent respectively 0.01 %, 0.1 % and 0.3 % of the brain volume.

Table 1
Respectively, the minimum, average and maximum absolute values of offsets with respect to the reference image obtained from image registration on μRaystation.

	Right-Left (mm ± 0.2)	Longitudinal (mm ± 0.2)	Anteroposterior (mm ± 0.2)
Brain	0.1/0.6/1.4	0.1/0.4/0.6	0.4/0.6/0.9
Lungs	0.1/1.0/2.0	1.6/2.3/3.4	0.0/0.2/0.4
Intestines	0.0/0.8/2.3	1.3/2.5/3.0	0.0/0.4/0.7

Table 2
Field dimensions at the target position used to verify the organ coverage of the heaviest mouse. The given values correspond to the optimal homogeneous field size defined from mouse-specific organ size O / Field size O with the addition of targeting margins m_T / Field size O with the addition of targeting margins m_T and respiratory margins m_R if applicable, respectively.

	Right-Left (mm ± 0.2)	Longitudinal (mm ± 0.2)	Anteroposterior (mm ± 0.2)
Brain	9.8/12.6	9.4/10.6	6.4/8.1
Lungs	17.0/21.0	13.0/19.8/21.5	16.0/16.8/17.4
Intestines	28.0/32.6	24.0/30.0	18.2/19.6

3.2. Impact of the dose delivery modality and the beam incidence

3.2.1. Conventional versus FLASH: Impact on beam characteristics and dosimetric impact of respiration

The collimator aperture must sufficient to compensate for the geometric penumbra, inducing edge profile degradation to obtain a flat lateral profile of the planned optimal field size. The penumbra simulation has been verified experimentally for FLASH (5000 Gy/s) and CONV (0.2 Gy/s) beam parameters with OC-1 films positioned at 10 cm after the collimator. The beam geometry is similar in both modalities (Fig. 2a). Then, the simulation was used to study the impact of the field size 4 cm away from the collimator. The geometric penumbra is defined in external radiotherapy as the distance between 20 % and 80 % of the profile's maximum. For the profiles measured at 10 cm from the collimator exit (15 mm aperture), the penumbra is equal to 1.7 mm. In comparison, at 4 cm from the collimator, the penumbra is reduced to 0.6 mm for the collimator with 15 and 30 mm apertures, respectively, of the order of magnitude of field sizes for the brain and intestines. Hence, since the collimator size setting precision is 1 mm, the addition of 1 mm on each border of the optimal field size required will give the collimator aperture.

In addition, Fig. 2b compares CONV and FLASH irradiation modes regarding in-depth dose distribution measured with an ionization chamber in a water tank. Until the maximum Bragg peak, the differences between the two modes stayed below 1 %. The increased differences in the Bragg peak fall-out are driven mainly by the chamber's 250 μm of position uncertainty. Since no changes in the beam characteristics have been observed between FLASH and CONV modes, the phantom and mice simulations will be performed with the same Monte Carlo model of the beamline.

Fig. 3 shows the dose-volume histograms (DVH) obtained by Monte Carlo simulations on the MOBY digital preclinical phantom and extracted from μRaystation. For posterior irradiation (Fig. 3a), the respiratory phase has no significant impact on the dose distribution. Differences less than 1 % have been observed in the mean dose and HI98. HI98 increased from 20.4 % to 21.4 % between inflate and deflate for both lungs reunited, from 12.9 % to 13.4 % for the right lung and from 21.3 % to 21.8 % for the left lung. Conversely, DVH shifts during the deflation phase are observed for lateral irradiation (Fig. 3b), reflecting an increase in the absorbed dose in the organ. The impact of the respiration cycle on the homogeneity index of lateral irradiation (entrance on the left side) in Fig. 3b is also around 1 % with values in the inflation phase equals to 20.3 %, 17.6 % and 10.2 %, versus 21.4 %, 16.5 % and 10.5 % in the deflation phase, for both lungs, exit lung and entrance lung, respectively. However, the mean dose difference between full inspiration (inflate) and expiration (deflate), equaling + 0.9 % for the entrance lung (left), + 2.3 % for both lungs reunited, and + 2.9 % in the exit lung (right), is significant and reflects the impact of the variation in volume and density of the first lung on dose distribution.

3.2.2. Impact of the beam incidence (lateral versus posterior)

The ranges of dimensions of the organs among 3 independent μCBCT of 11 mice, weighted between 19.4 g and 33.4 g, are given in Table 3. The beam propagation is orthogonal to the Right-Left/Longitudinal (head to feet) plane for posterior irradiation. The beam propagation is orthogonal to the Longitudinal/Anteroposterior plane for lateral irradiation. The corresponding volumes of the boxes, meant to simulate radiation fields, enclosing the organs of each mouse with respect to their body weight (w) are displayed in Supplementary (Suppl. Fig. S2). Linear least-square regression showed that for the brain, the box volume y_{Organ} is not correlated with the mouse weight $\left(y_{Brain} = 0.006 \times w + 0.357,\ R^2 = 0.27\right)$. This outcome is worthwhile because it enables a single field size for all mice. Conversely, for the lungs and the intestines, the field size should be adapted to weight to include inter-animal variation. Despite the limited data collection, a correlation can be found with the weight with $R^2 = 0.78$ and 0.88, respectively $\left(y_{Lungs} = 0.083 \times w + 0.853,\ y_{Intestines} = 0.323 \times w + 0.436\right)$ allowing to calculate the adequate beam size according to the weight.

Due to the mobility of the organs in the abdominal area, intestine irradiation often consists of whole abdomen irradiation [16]. In this case, the target is almost equal to the total body width. Only the

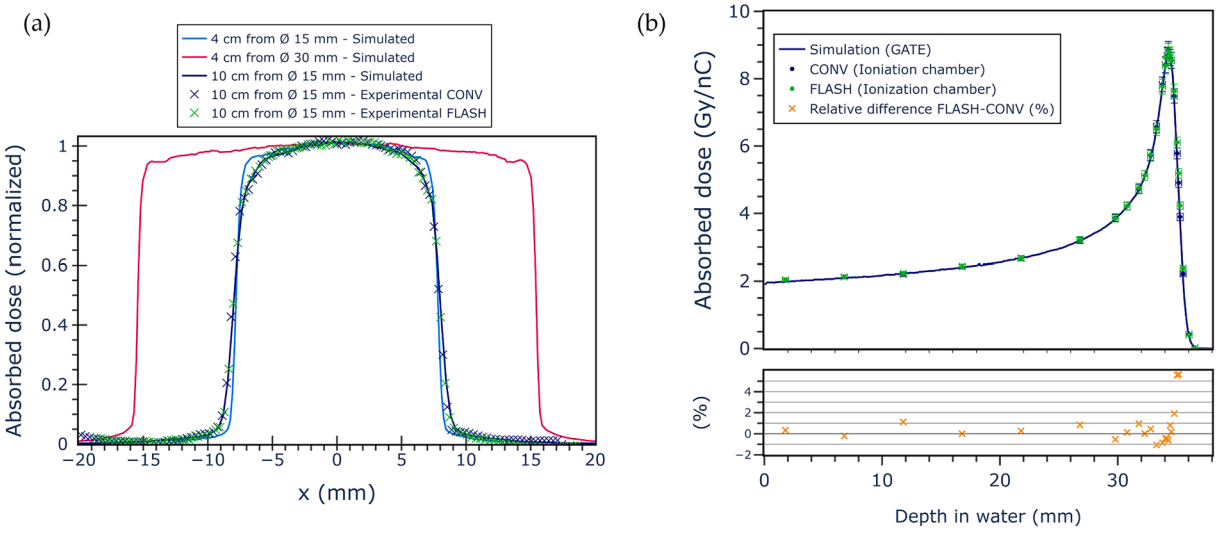

Fig. 2. Lateral profiles of the beam at the target position. Experimental points are from radiochromic OC-1 films. The simulation and experimental spatial resolution are 150 dpi. Statistical uncertainty on simulated dose is less than 2%, and experimental uncertainty on dose is 3%.

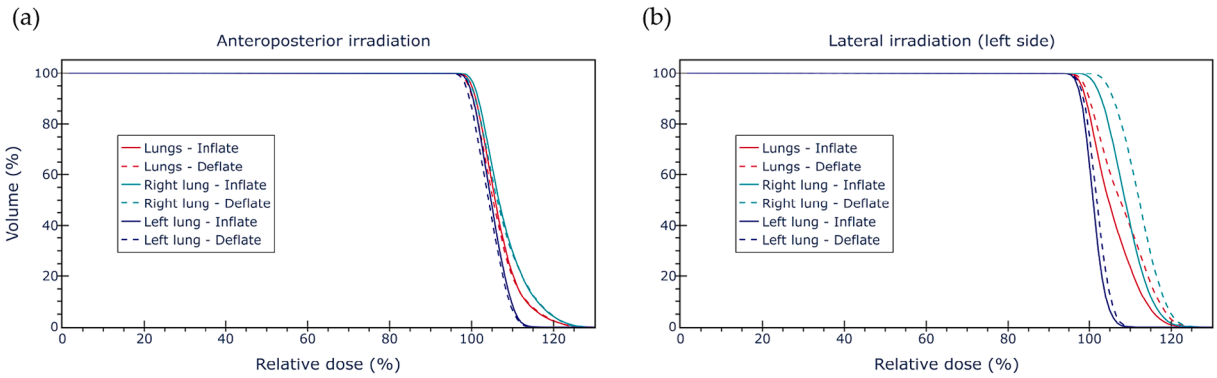

Fig. 3. Relative dose-volume histograms for posterior (a) and lateral (b) irradiation of lungs, at full inspiration and full expiration. For the lateral irradiation, the left lung is located on the beam entrance side and the right lung in the exit side.

Table 3
Ranges of dimensions for the brain, the lungs and the intestines in the three directions for eleven mice weighted between 19.4 and 33.4 g, and mean intra-individual deviations between the three μCBCT per mice.

	Right-Left (mm ± 0.2)	**Longitudinal** (mm ± 0.2)	**Anteroposterior** (mm ± 0.2)
Brain	[9.0–9.8]	[7.4–9.4]	[5.6–7.2]
	$\sigma_{mean} = 0.1$	$\sigma_{mean} = 0.1$	$\sigma_{mean} = 0.2$
Lungs	[13.8–17.0]	[10.6–14.0]	[12.0–17.0]
	$\sigma_{mean} = 0.2$	$\sigma_{mean} = 0.6$	$\sigma_{mean} = 0.9$
Intestines	[22.2–29.2]	[17.0–24.0]	[14.4–18.8]
	$\sigma_{mean} = 0.9$	$\sigma_{mean} = 0.8$	$\sigma_{mean} = 0.6$

Table 4
Dosimetric quantities for tagets (HI98) and OAR (mean dose $\bar{D}$ and dose received by 2% of the volume $D_{2\%}$) during lateral or posterior brain and lungs irradiations.

Brain irradiation		
Mouse weight $w = 33.4$ g		
Beam incidence	Lateral	Posterior
Brain	HI98 = 9.9%	HI98 = 6.1%
Buccal cavity	$\bar{D} < 1\%*\bar{D}_{Brain}$	$\bar{D} = 21\%*\bar{D}_{Brain}$
Lungs irradiation		
Mouse weight $w = 20.4$ g		
Beam incidence	Lateral (left side)	Posterior
Lungs	HI98 = 17.3%	HI98 = 12.9%
Left lung	HI98 = 7.3%	HI98 = 9.4%
Right lung	HI98 = 13.5%	HI98 = 12.6%
Heart	$\bar{D}=98\%*\bar{D}_{Lungs}$	$\bar{D}=107\%*\bar{D}_{Lungs}$
Spinal cord	$D_{2\%}= 93\%*D_{2\%Lungs}$	$D_{2\%}=94\%*D_{2\%Lungs}$
Mouse weight $w = 33.4$ g		
Beam incidence	Lateral (left side)	Posterior
Lungs	HI98 = 22.5%	HI98 = 14.8%
Left lung	HI98 = 9.5%	HI98 = 10.6%
Right lung	HI98 = 17.8%	HI98 = 15.7%
Heart	$\bar{D}=98\%*\bar{D}_{Lungs}$	$\bar{D}=109\%*\bar{D}_{Lungs}$
Spinal cord	$D_{2\%}=92\%*D_{2\%Lungs}$	$D_{2\%}=98\%*D_{2\%Lungs}$

posterior irradiation of the lightest mouse is, a priori, compatible with Bragg plateau conditions. For the lungs, even considering their relatively low mass density, the total body width (muscle and bones) compromises the homogeneity, and the dosimetric outcome is challenging to predict. So, the comparison will be performed on the lightest and the heaviest mouse. Finally, for the brain, the comparison will be made on the heaviest mouse as the brain and head sizes are not significantly impacted by ageing (Suppl. Fig. S2).

The dose distributions have been simulated on the selected mice, and the dosimetric quantities extracted from μRaystation for the three target organs are displayed in Table 4, and a visualization is displayed in Supplementary (Suppl. Fig. S3). In addition, considering the posterior irradiation of the abdomen of the lightest mouse, the HI98 in the intestines equals 25 %.

3.3. *In vivo dosimetry*

3.3.1. *LET dependence of OC-1 films*

First, the quenching relationship with protons dose-averaged LET (LET_d) of OC-1 films was characterized by an in-depth dose measure with the calibrated plane-parallel ionization chamber (Markus Advanced, TRS-398) in RW3 slabs. The depth dose curve and the corresponding LET_d are displayed in Fig. 4a. A correction up to 12.5 % must be applied within the Bragg peak region ($LET_d > 5$ keV/μm). This result is in the same order that was found by Anderson *et al.* [35] with EBT3 Gafchromic films (10 % for $LET_d = 5$ keV/μm to 20 % for $LET_d = 8$ keV/μm). Then, a similar linear relation for film under-response was derived by linear least-square regression (Fig. 4b):

$$U = \left[(-6.6 \pm 0.7).10^{-3}\mu\text{m.keV}^{-1}\right] \times LET_d + (1.00 \pm 0.01)(R^2 = 0.91).$$

If the LET_d value remains below 5 keV/μm, the correction is lower than the experimental uncertainty of the dose; then the correction is not mandatory.

This correction was experimentally verified with calibrated tissue substitutes and RW3. Dose maps and corresponding LET_d maps were simulated. For each dose pixel on the simulated films, the linear correction was applied to compare the simulated and the experimental films by 2D local gamma index (Table 5). The precision of experimental phantom alignment is 0.5 mm. This value is the selected distance criterion (*DTA*), and after normalization on a low LET_d region, the dose difference (*DD*) was set to 1 %. The dose threshold was set to 10 % of the maximum displayed dose to avoid influence from the unirradiated surface and film surface defects.

The satisfactory agreement between simulated and experimental films placed after a complex geometry indicates that the films are suitable for *in vivo* dosimetry and targeting verification with appropriate quenching linear correction (Table 4). However, even after correction, some deviations remain, particularly in the higher LET areas, and carrying out another extensive study in this range could improve this method for the OC-1 films.

3.3.2. *Feasibility of using OC-1 films for in vivo dosimetry in mouse*

To validate the workflow detailed in Fig. 1c and verify the feasibility of the *in vivo* dosimetry method with OC-1 films, one of the sacrificed mice from the imaging study was irradiated at ARRONAX with our set-

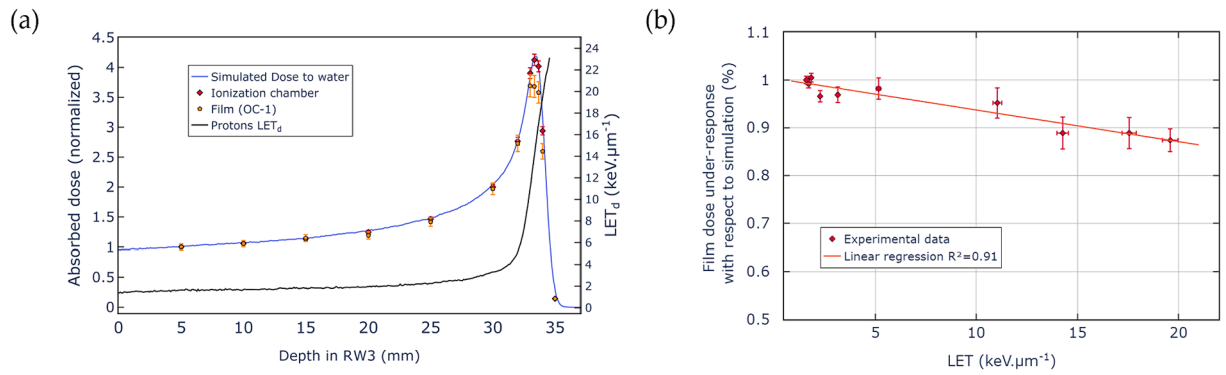

Fig. 4. (a) In-depth measurement of the quenching effect of OC-1 films in RW3 slabs, (b) linear relationship between film under-response and proton LET$_d$ in RW3.

Table 5
2D local gamma index pass rate (DD 1 % and DTA 0.5 mm) for various phantoms, with and without LET$_d$ correction.

Cylinders	LET$_d$ > 5 keV/µm	Quenching correction	Pass rate (%)
Adipose and B-200	No	No	99.3
Adipose and B-200	No	Yes	99.4
B200 + 5 mm RW3	Yes	No	82.1
B200 + 5 mm RW3	Yes	Yes	96.6

up. Fig. 5a is a photograph of the film downstream of the mouse, and Fig. 5b is the 2D plot of the simulated film, both showing the skull footprint in a darker shade. The simulated and the experimental films placed downstream of the brain during lateral irradiation were compared using the local gamma index metrics. The DTA was updated using the precision of the positioning determined in section 3.1 choosing the Euclidian distance formed by the longitudinal and posterior offsets equal to 1 mm. The dose difference criterion and the threshold were kept at 1 % and 10 %, respectively. No quenching correction was applied since the LET$_d$ stayed below 5 keV/µm. The gamma analysis, whose 2D failed points map is in Fig. 5c, concluded that 98.6 % of the pixels in the simulation tested matched the experimental film within these tolerances, confirming the accuracy of the animal position on the ARRONAX beamline.

4. Discussion

The repositioning system enables the animal to be held in a position suitable for irradiation (paws kept out of the irradiation field) without causing injury. Target margins were defined for the brain, the lungs and the intestines from ten repositioning sessions without the help of the imaging system to simulate the positioning in ARRONAX. In addition, the repositioning dependency on the operator has been observed for the brain on the right-left and anteroposterior directions due to the muzzle position in the anaesthetic nozzle. Hence, the same operator needs to perform both image and irradiation positioning. Moreover, high minimal values were observed for lungs and intestines in the longitudinal direction, traducing a systematic deviation with the reference image. Image analysis showed an abnormal arching of the neck for the reference positioning, which did not however have any impact on the positioning of the brain. However, this substantially increased the value of the margins found, which, if we reduce the minimum deviation to 0, would be around 0.7 mm on average for the lung and 1.2 mm for the intestines. Moreover, relatively large targeting margins are observed and could be reduced, especially for the non-moving brain, with set-up improvements. Head rotations can be limited by adding a tooth bar to the current anaesthetic muzzle holder and, or even loose ear bars for vertical irradiation, as used in preclinical stereotaxic irradiations or imaging studies [36,37]. Furthermore, the respiratory margins were obtained from fluoroscopic images in the longitudinal (1.7 mm) and posterior (0.6 mm) directions. To avoid coverage loss during the respiratory cycle, these respiratory amplitudes have been taken on the heavier mouse of the cohort (33.4 g), whose lung size is maximal and corresponding respiratory amplitudes are assumed maximal. Moreover, no correlation between targeting margins and mouse weight was observed.

While limiting the animal rotation, the repositioning system does not prevent entirely the targets rotation. However, we show that the defined margins ensure the target coverage. Indeed, the target volume is always enclosed for the lungs and intestines. The head is more difficult to align

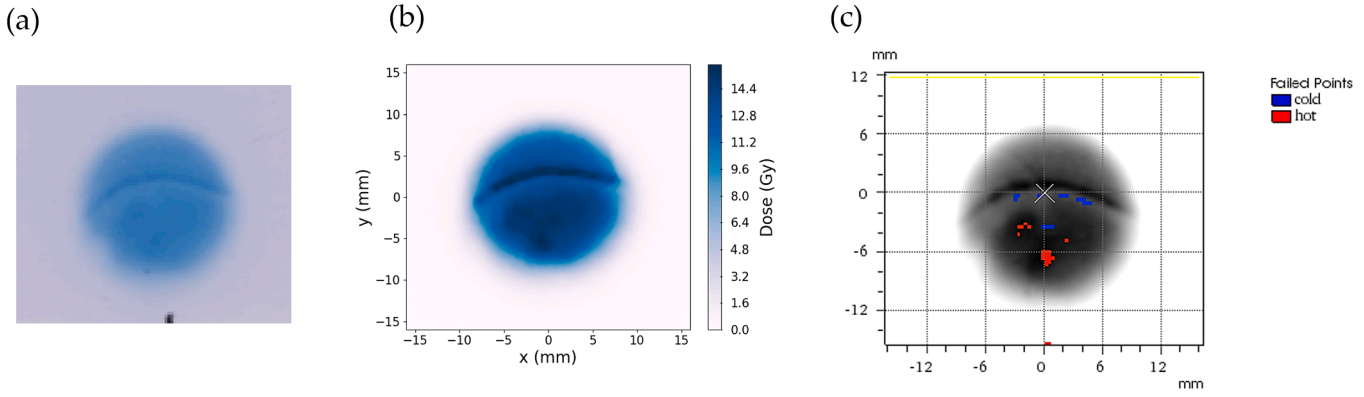

Fig. 5. (a) Experimental and (b) simulated OC-1 films from mouse brain irradiation and (c) 2D Gamma index failed points map between simulated and experimental back films. Blue points indicate under-dosage, and the red over-dosage. (For interpretation of the references to colour in this figure legend, the reader is referred to the web version of this article.)

and prone to rotations. Consequently, we observed a brain uncovering in three of the ten studied cases. Nevertheless, the uncovered brain volumes are very small (<0.5 %) and not significant. In the two first cases, a negative pitch has been recorded on two images, resulting in the uncovering of the upper lower part of the brain in case of lateral beam. In the third case, a negative head roll towards the right side uncovers the lower right part of the brain. Contrary to the first case, this cannot be solved easily by slightly opening the corresponding side of the collimator because of the sensitive buccal region underneath. To improve this, a system of three cross lasers has been set in ARRONAX to help target the brain more effectively, guaranteeing the same height for both ears and horizontality of the brain.

In an ideal situation, the dose delivery modality should not impact the dose distribution. If not, the differences have to be considered. In our case, the dose distribution is similar for both conventional and ultra-high dose rates, allowing the use of a single Monte Carlo model of the beamline. Due to the very short beam duration (millisecond) in FLASH-RT compare with the respiratory cycle duration (second), the respiratory phase could impact the dose distribution. We show that for posterior irradiation, the respiratory phase has no significant impact on the dose distribution. However, for a lateral irradiation, the mean dose of the exit lung and the entire lungs are significantly impacted. In this last case, only the entrance lung can be considered for biological analysis due to the modification of the dose delivered to the exit lung. Moreover, the most potentially detrimental case for lateral irradiation was studied, where the largest lung, the right lung, is placed on the exit side of the beam, protecting the heart placed on the side of the beam entrance. Finally, in this lateral case, we observed that the deflate phase gives higher homogeneity than the inspiration, especially for the exit of the right lung. An explanation is that, during inspiration, the outer part of the lung close to the rib cage ends up behind the liver, and this area finds itself much further along the Bragg curve, where the deposited energy increases.

Lateral and posterior irradiations were compared for brain and lungs targeting. As expected from the results in Table 3, whole organ irradiation according to the posterior direction is beneficial compared to the right-left direction because most organ sizes are smaller in that direction, decreasing dose heterogeneity (-4% for the brain and −4% to −8% for both lungs reunited). Besides, all radiosensitive organs at risk studied, the buccal cavity (-20 %), the heart (-9%) and the spinal cord (-1% to - 6 % for the heaviest mouse), could benefit from lateral irradiation compared to posterior irradiation. For the brain, the lateral incidence provides the best compromise with a high protection of the buccal cavity and an acceptable homogeneity. The impact of the mouse weight on the dose homogeneity of the lungs is mainly driven by the exit lungs (right in this case) for lateral irradiation and the right lung, the largest one, for posterior irradiation. Therefore, biological analysis should be performed on the entrance lung during lateral irradiation with a dose considering the increased dose taken by the other lung. For the posterior irradiation, the dose homogeneity is better on the left lung, and unilateral irradiation on the left lung could be envisioned. However, because of the heart located underneath, right-sided irradiation on a juvenile mouse should improve the homogeneity while decreasing the dose to the heart. The large dimensions of the intestines in right-left direction exclude the lateral irradiation for this target. The HI98 computed for the whole abdomen was equal to 25 % for the posterior irradiation of the lightest mouse, due to the difference of width between the flank (6 mm) and the center (18 mm). Biological analysis should consider the inherent dose uncertainty caused by the increasing dose along the Bragg curve. The best incidence for intestine irradiation is an anterior beam, but requires to design a specific repositioning system. The use of a Spread-Out Bragg Peak (SOBP) could drastically improve the homogeneity for lungs and intestines particularly [38].

Finally, we show that *in vivo* dosimetry is feasible with OC-1 films placed behind the mouse but requires a correction of the LET impact. Ideally, the 3D onboard imager, providing information about the mouse position and the image for the dosimetric calculation, is positioned directly on the proton beamline. This solution was adopted by Kim et al. [6], using a SARRP (Small Animal Radiation Research Platform) small animal irradiator. In this case, the correspondence of the treatment and imaging isocenters must be carefully controlled before irradiation. Kim *et al.* obtained a misalignment of 2.67 ± 0.38 mm between the two isocenters mainly due to the SARRP displacement on rails. However, a dedicated quality control process and a correction method have been developed and implemented, providing a final x-ray-proton beam alignment accuracy of 0.12 ± 0.04 mm. Such a solution is not always viable because of the cost or space required. Alternatively, as is usual for clinical LINACs, the treatment beam can be used directly to check the positioning. In preclinical proton therapy, this method of proton radiography has been successfully implemented by Schneider and his team [39]. They obtained a sub-millimeter accuracy in the calculated beam target coordinates (<0.41 ± 0.19 mm) for an absorbed dose < 23 mGy. Precisely, they reported for mice inter and intra-observer mean variations of 0.26 ± 0.10 mm and 0.22 ± 0.10 mm, respectively. These values are, as anticipated, lower than our corresponding values (mean values of 0.4 ± 0.2 mm and 0.6 ± 0.2 mm in longitudinal and anteroposterior direction, respectively, and maximal values of 0.6 ± 0.2 and 0.9 ± 0.2 mm), showing the benefits of an onboard imaging system. One must consider that in our study, as for a realistic treatment, all deviations between repositioning were assessed with respect to the first reference image and not relative to each other. Furthermore, this system is envisioned because of the perspective of calibration for in vivo dosimetry for transmission beam irradiation. However, because of the lower beam energy available, a feasibility study must be carried out to validate the achievement of a satisfactory contrast-spatial resolution-dose balance under these conditions.

5. Conclusion

This study investigates dosimetric considerations for performing preclinical irradiations with a similar approach to the clinical practice (target sizes, targeting precision and dose distribution homogeneity) in a research facility not equipped with image guidance system. In particular, the repositioning system, similar to those used for patients, ensures targeted irradiation of internal organs, such as the brain, lungs or intestines, with optimum margins to ensure satisfactory dose coverage.

Besides, the CONV and FLASH beam characteristics, including geometry, have been measured experimentally and led to using a single Monte Carlo model of the beamline. Moreover, the maximal impact of the respiratory motion, possibly even more significant in FLASH-RT with 65 MeV protons, has been evaluated on a digital mouse phantom (MOBY). It was found that the impact is negligible for posterior irradiation and the entrance lung during lateral irradiation. Also, two beam incidences for mouse irradiations of the brain, lungs and intestines have been compared. Regarding whole organs irradiations, posterior incidence significantly decreases the dose heterogeneity in the target. However, due to the potential toxicities to sensitive organs in the irradiation field, lateral irradiation can be envisioned, with an adapted dose plan and choice of the organ part to be analyzed, as satisfactory homogeneity can be achieved for the brain and the lungs on small mice. Moreover, to achieve a satisfactory homogeneity in the case of intestines, especially for whole abdomen irradiation, the use of a Spread-Out Bragg Peak (SOBP) could be beneficial [38]. In addition, a SOBP would spare the contralateral lung in the case of lateral irradiation of the lungs, while preserving homogeneity in the entrance lung.

Furthermore, new films OC-1 LET-related quenching have been characterized and used to correct the film response for comparison with Monte Carlo simulations. Moreover, the films enable targeting to be verified, providing an experimental comparison for assessing the error in the simulated dose distribution in the organ, which is mandatory to enable the dose–effect correlation.

This study confirms the feasibility, both from technical and

dosimetric perspectives, of performing CONV and FLASH accurately targeting the irradiation of various internal organs of small animals in a research platform without image guidance. The presented methodology, involving a Monte Carlo model of our beamline, the use of OC-1 radiochromic films and a well-defined protocol for mice positioning, has been validated from end-to-end with a dead mouse and could be reproduced by any team keen to perform targeted irradiation without image guidance. In the future, this in vivo dosimetry method with OC-1 films will be carried out systematically for future radiobiology studies on mice, enabling an overall assessment of the geometric and dosimetric accuracy of the irradiation.

Ethical statement

Animal experiments were evaluated and approved by the local Ethics Committee in compliance with the 2010/63/EU regulations.

Funding

The cyclotron Arronax is supported by CNRS, Inserm, Nantes University, the Regional Council of Pays de la Loire, local authorities, the French government and the European Union. This work has been, in part, supported by a grant from the French National Agency for Research called “Investissements d’Avenir”, Equipex Arronax-Plus ANR-11-EQPX-0004, and with financial support from Inserm Cancer. We thank Association Vendéenne de Lutte contre le Cancer and Fondation Groupama for their support.

Conflicts of interest

The authors declare no conflict of interest. The funders had no role in the design of the study; in the collection, analyses, or interpretation of data; in the writing of the manuscript, or in the decision to publish the results.

CRediT authorship contribution statement

Manon Evin: Conceptualization, Methodology, Software, Validation, Formal analysis, Investigation, Data curation, Writing – original draft, Writing – review & editing, Visualization. **Charbel Koumeir:** Methodology, Investigation, Data curation, Writing – review & editing, Visualization, Supervision. **Arthur Bongrand:** Software, Writing – review & editing. **Gregory Delpon:** Conceptualization, Validation, Resources, Writing – review & editing, Visualization, Project administration, Funding acquisition. **Ferid Haddad:** Resources, Writing – review & editing, Funding acquisition. **Quentin Mouchard:** Investigation, Data curation, Writing – review & editing, Visualization. **Vincent Potiron:** Data curation, Writing – review & editing. **Gaëlle Saade:** Data curation, Writing – review & editing. **Noël Servagent:** Data curation, Writing – review & editing. **Daphnée Villoing:** Conceptualization, Writing – review & editing. **Vincent Métivier:** Investigation, Resources, Writing – review & editing, Visualization, Supervision, Project administration, Funding acquisition. **Sophie Chiavassa:** Conceptualization, Methodology, Software, Validation, Formal analysis, Investigation, Data curation, Writing – original draft, Writing – review & editing, Visualization, Supervision.

Declaration of competing interest

The authors declare that they have no known competing financial interests or personal relationships that could have appeared to influence the work reported in this paper.

Data Availability

Data available on request due to restrictions eg privacy or ethical. The data presented in this study are available on request from the corresponding author. The data are not publicly available due to their extended size, incompatible with online upload.

Appendix A. Supplementary data

Supplementary data to this article can be found online at https://doi.org/10.1016/j.ejmp.2024.103332.

References

[1] Tillner F, Thute P, Bütof R, Krause M, Enghardt W. Pre-clinical research in small animals using radiotherapy technology–a bidirectional translational approach. Z Med Phys 2014;24(4):335–51. https://doi.org/10.1016/j.zemedi.2014.07.004.
[2] Verhaegen F, Dubois L, Gianolini S, et al. ESTRO ACROP: technology for precision small animal radiotherapy research: optimal use and challenges. Radiother Oncol 2018;126(3):471–8. https://doi.org/10.1016/j.radonc.2017.11.016.
[3] Delpon G, Frelin-Labalme AM, Heinrich S, Beaudouin V, Noblet C, Begue M, Le Deroff C, Pouzoulet F, Chiavassa S. « Radiothérapie guidée par l’image pour les petits animaux: une nouvelle ère pour les études précliniques » [Small animal image-guided radiotherapy: A new era for preclinical studies]. Cancer Radiother. 2016 Feb;20(1):43-53. French. doi: 10.1016/j.canrad.2015.08.001. Epub 2016 Feb 5. PMID: 26856635.
[4] Hill MA, Thompson JM, Kavanagh A, et al. The development of technology for effective respiratory-gated irradiation using an image-guided small animal irradiator. Radiat Res 2017;188(3):247–63. https://doi.org/10.1667/RR14753.1.
[5] Frelin AM, Beaudouin V, Le Deroff C, Roger T. Implementation and evaluation of respiratory gating in small animal radiotherapy. *Phys Med Biol.* 2018;63(21): 215024. Published 2018 Oct 30. doi:10.1088/1361-6560/aae760.
[6] Kim MM, Irmen P, Shoniyozov K, et al. Design and commissioning of an image-guided small animal radiation platform and quality assurance protocol for integrated proton and x-ray radiobiology research. *Phys Med Biol.* 2019;64(13): 135013. Published 2019 Jul 4. doi:10.1088/1361-6560/ab20d9.
[7] Favaudon V, Caplier L, Monceau V, et al. Ultrahigh dose-rate FLASH irradiation increases the differential response between normal and tumor tissue in mice [published correction appears in Sci Transl Med. 2019 Dec 18;11(523):]. *Sci Transl Med.* 2014;6(245):245ra93. doi:10.1126/scitranslmed.3008973.
[8] Esplen N, Mendonca MS, Bazalova-Carter M. Physics and biology of ultrahigh dose-rate (FLASH) radiotherapy: a topical review. *Phys Med Biol.* 2020;65(23):23TR03. Published 2020 Dec 4. doi:10.1088/1361-6560/abaa28.
[9] Schüler E, Trovati S, King G, et al. Experimental platform for ultra-high dose rate FLASH irradiation of small animals using a clinical linear accelerator. Int J Radiat Oncol Biol Phys 2017;97(1):195–203. https://doi.org/10.1016/j.ijrobp.2016.09.018.
[10] Lempart M, Blad B, Adrian G, et al. Modifying a clinical linear accelerator for delivery of ultra-high dose rate irradiation. Radiother Oncol 2019;139:40–5. https://doi.org/10.1016/j.radonc.2019.01.031.
[11] Patriarca A, Fouillade C, Auger M, et al. Experimental set-up for FLASH proton irradiation of small animals using a clinical system. Int J Radiat Oncol Biol Phys 2018;102(3):619–26. https://doi.org/10.1016/j.ijrobp.2018.06.403.
[12] Koumeir C, De Nadal V, Cherubini R, et al. The radiobiological platform at arronax. Radiat Prot Dosimetry 2019;183(1–2):270–3. https://doi.org/10.1093/rpd/ncy301.
[13] Saade G, Bogaerts E, Chiavassa S, et al. Ultrahigh-Dose-Rate Proton Irradiation Elicits Reduced Toxicity in Zebrafish Embryos. *Adv Radiat Oncol.* 2022;8(2): 101124. Published 2022 Nov 19. doi:10.1016/j.adro.2022.101124.
[14] Ghannam Y, Chiavassa S, Saade G, et al. First evidence of in vivo effect of FLASH radiotherapy with helium ions in zebrafish embryos. Radiother Oncol 2023;187: 109820. https://doi.org/10.1016/j.radonc.2023.109820.
[15] Bongrand A, Koumeir C, Villoing D, et al. A Monte Carlo Determination of Dose and Range Uncertainties for Preclinical Studies with a Proton Beam. *Cancers (Basel).* 2021;13(8):1889. Published 2021 Apr 15. doi:10.3390/cancers13081889.
[16] Diffenderfer ES, Verginadis II, Kim MM, et al. Design, implementation, and in vivo validation of a novel proton FLASH radiation therapy system. Int J Radiat Oncol Biol Phys 2020;106(2):440–8. https://doi.org/10.1016/j.ijrobp.2019.10.049.
[17] Montay-Gruel P, Petersson K, Jaccard M, et al. Irradiation in a flash: unique sparing of memory in mice after whole brain irradiation with dose rates above 100Gy/s. Radiother Oncol 2017;124(3):365–9. https://doi.org/10.1016/j.radonc.2017.05.003.
[18] Poirier F., Blain G., Bulteau-harel F., Fattahi M., Goiziou X., Haddad F., Koumeir C., Letaeron A., Vandenborre J. The Pulsing Chopper-Based System of the Arronax C70XP Cyclotron; JACOW Publishing: Geneva, Switzerland, 2019; pp. 1948–1950. doi: 10.18429/JACOW-IPAC2019-TUPTS008.
[19] Bongrand A, Koumeir C, Villoing D, Guertin A, Haddad F, Metivier V, Poirier F, Potiron V, Servagent N, Supiot S, Delpon G, Chiavassa S, EPD097 - Maximization of the dose homogeneity in the Plateau for a low-energy preclinical proton beam line, Phys Med, Volume 94, Supplement, 2022, Page S100, ISSN 1120-1797, DOI: 10.1016/S1120-1797(22)01668-4.
[20] Chiavassa S, Nilsson R, Clément-Colmou K, Potiron V, Delpon G, Traneus E. Validation of the analytical irradiator model and Monte Carlo dose engine in the small animal irradiation treatment planning system μ-RayStation 8B. *Phys Med Biol.* 2020;65(3):035006. Published 2020 Jan 24. doi:10.1088/1361-6560/ab6155.

[21] Sarrut D, Bardiès M, Boussion N, et al. A review of the use and potential of the GATE Monte Carlo simulation code for radiation therapy and dosimetry applications. Med Phys 2014;41(6):064301. https://doi.org/10.1118/1.4871617.
[22] Arce P, Bolst D, Bordage MC, et al. Report on G4-med, a Geant4 benchmarking system for medical physics applications developed by the Geant4 medical simulation benchmarking group. Med Phys 2021;48(1):19–56. https://doi.org/10.1002/mp.14226.
[23] Winterhalter C, Taylor M, Boersma D, et al. Evaluation of GATE-RTion (GATE/Geant4) Monte Carlo simulation settings for proton pencil beam scanning quality assurance. Med Phys 2020;47(11):5817–28. https://doi.org/10.1002/mp.14481.
[24] Noblet C, Delpon G, Supiot S, Potiron V, Paris F, Chiavassa S. A new tissue segmentation method to calculate 3D dose in small animal radiation therapy. *Radiat Oncol.* 2018;13(1):32. Published 2018 Feb 26. doi:10.1186/s13014-018-0971-8.
[25] International Commission on Radiation Units and Measurements (ICRU). Report 44. Tissue substitutes in radiation dosimetry. Washington: International Commission on Radiation Units and Measurements; 1989.
[26] International Commission on Radiation Units and Measurements (ICRU). Report 46. Photon, electron, proton and neutron interaction data for body tissues. Washington: International Commission on Radiation Units and Measurements; 1992.
[27] El Naqa I, Kawrakow I, Fippel M, et al. A comparison of Monte Carlo dose calculation denoising techniques. Phys Med Biol 2005;50(5):909–22. https://doi.org/10.1088/0031-9155/50/5/014.
[28] Cavallone M, Gonçalves Jorge P, Moeckli R, et al. Determination of the ion collection efficiency of the Razor Nano Chamber for ultra-high dose-rate electron beams. Med Phys 2022;49(7):4731–42. https://doi.org/10.1002/mp.15675.
[29] Segars WP, Tsui BM, Frey EC, Johnson GA, Berr SS. Development of a 4-D digital mouse phantom for molecular imaging research. Mol Imaging Biol. 2004 May-Jun; 6(3):149-59. DOI: 10.1016/j.mibio.2004.03.002. PMID: 15193249.
[30] van der Heyden B, van Hoof SJ, Schyns LE, Verhaegen F. The influence of respiratory motion on dose delivery in a mouse lung tumour irradiation using the 4D MOBY phantom. Br J Radiol 2017;90(1069):20160419. https://doi.org/10.1259/bjr.20160419.
[31] Villoing D, Koumeir C, Bongrand A, et al. Technical note: proton beam dosimetry at ultra-high dose rates (FLASH): evaluation of GAFchromic™ (EBT3, EBT-XD) and OrthoChromic (OC-1) film performances. Med Phys 2022;49(4):2732–45. https://doi.org/10.1002/mp.15526.
[32] Niroomand-Rad A, Chiu-Tsao ST, Grams MP, et al. Report of AAPM task group 235 radiochromic film dosimetry: an update to TG-55. Med Phys 2020;47(12): 5986–6025. https://doi.org/10.1002/mp.14497.
[33] An International Code of Practice for Dosimetry based on absorbed dose to water IAEA Tech. Series No.398, Absorbed dose determination in external beam radiotherapy. Vienna: IAEA; 2000.
[34] Guan F, Peeler C, Bronk L, et al. Analysis of the track- and dose-averaged LET and LET spectra in proton therapy using the geant4 Monte Carlo code [published correction appears in Med Phys. 2018 Mar;45(3):1302]. *Med Phys.* 2015;42(11): 6234-6247. doi:10.1118/1.4932217.
[35] Anderson SE, Grams MP, Wan Chan Tseung H, Furutani KM, Beltran CJ. A linear relationship for the LET-dependence of Gafchromic EBT3 film in spot-scanning proton therapy. *Phys Med Biol.* 2019;64(5):055015. Published 2019 Mar 7. doi: 10.1088/1361-6560/ab0114.
[36] Espinosa-Oliva AM, de Pablos RM, Herrera AJ. Intracranial injection of LPS in rat as animal model of neuroinflammation. Methods Mol Biol 2013;1041:295–305. https://doi.org/10.1007/978-1-62703-520-0_26.
[37] Petiet A, Delatour B, Dhenain M. Models of neurodegenerative disease - Alzheimer's anatomical and amyloid plaque imaging. Methods Mol Biol 2011;771: 293–308. https://doi.org/10.1007/978-1-61779-219-9_16.
[38] Kim MM, Verginadis II, Goia D, et al. Comparison of FLASH Proton Entrance and the Spread-Out Bragg Peak Dose Regions in the Sparing of Mouse Intestinal Crypts and in a Pancreatic Tumor Model. *Cancers (Basel).* 2021;13(16):4244. Published 2021 Aug 23. doi:10.3390/cancers13164244.
[39] Schneider M, Bodenstein E, Bock J, et al. Combined proton radiography and irradiation for high-precision preclinical studies in small animals. *Front Oncol.* 2022;12:982417. Published 2022 Aug 31. doi:10.3389/fonc.2022.982417.